Dynamic behaviors of a laser-induced bubble and transition mechanism of collapse patterns in a tube

Hongchen Li (iD), Jian Huang, Xianqian Wu (iD), Jian Zhang, Jingzhu Wang, Yiwei Wang, and Chenguang Huang

COLLECTIONS

Paper published as part of the special topic on Chemical Physics, Energy, Fluids and Plasmas, Materials Science and Mathematical Physics

View Online   Export Citation   CrossMark

ARTICLES YOU MAY BE INTERESTED IN

Simulation of bubble expansion and collapse in the vicinity of a free surface
Physics of Fluids **28**, 052103 (2016); https://doi.org/10.1063/1.4949354
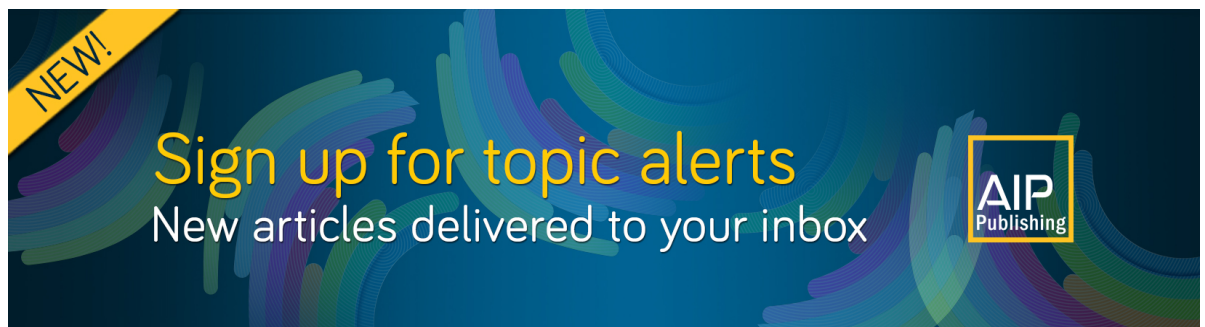
Laser induced cavitation: Plasma generation and breakdown shockwave
Physics of Fluids **31**, 103302 (2019); https://doi.org/10.1063/1.5119794

Numerical investigation of bubble dynamics at a corner
Physics of Fluids **32**, 053306 (2020); https://doi.org/10.1063/1.5140740

Dynamic behaviors of a laser-induced bubble and transition mechanism of collapse patterns in a tube

View Online   Export Citation   CrossMark

Hongchen Li,[1,2] Jian Huang,[2] Xianqian Wu,[1,2] Jian Zhang,[3] Jingzhu Wang,[1,2] Yiwei Wang,[1,2,a)] and Chenguang Huang[1,2]

AFFILIATIONS

[1] Key Laboratory for Mechanics in Fluid Solid Coupling Systems, Institute of Mechanics, Chinese Academy of Sciences, No. 15, Beisihuan West Road, Haidian District, Beijing 100190, China
[2] School of Engineering Science, University of Chinese Academy of Sciences, No. 19 (A), Yuquan Road, Shijingshan District, Beijing 100049, China
[3] Beijing Electro-mechanical Engineering Institude, No. 40, Yungang North Street, Fengtai District, Beijing 100074, China

[a)] Author to whom correspondence should be addressed: wangyw@imech.ac.cn

ABSTRACT

The pulsation of cavitation bubbles under constraint conditions has complex dynamic characteristics and has been widely applied in various fields, such as liquid pumping, underwater propulsion, and clinical applications. In this study, the dynamic behaviors of a laser-induced bubble in a tube are investigated under different initial conditions. A high-speed optical visualization is carried out in the experiments. The numerical simulation based on the volume-of-fluid method is implemented on the open source code OpenFOAM. From the experimental observation and numerical analysis, an axial jet pointing toward the front end of the tube is generated during bubble shrinkage. According to the type of the axial jet, the collapse patterns are classified into three regimes: one-dimensional, transitional, and three-dimensional. Furthermore, it is also found that the normalized initial energy of the bubble and the length-to-diameter ratio affect the maximum length and the pulsation period of the bubble. Finally, the transition mechanism of the collapse patterns from one dimension to three dimension is obtained through a phase diagram by combining experimental observations with numerical simulation.

I. INTRODUCTION

The phenomenon of cavitation has been observed in the fields of industrial cleaning,[1,2] biomedical engineering,[3,4] chemical reactions,[5,6] marine engineering,[7,8] and other applications.[9,10] Its dynamic behaviors have been studied in detail experimentally, theoretically, and numerically. In a uniform flow, a cavitation bubble can remain spherical during volume oscillation. For the constraint conditions, the pulsation of cavitation bubbles has more complex dynamic characteristics, which appear more frequently in the practical application.[11–13] Kornfeld and Suvorov[14] were the first to propose that the cavitation bubble close to the rigid wall deformed besides the periodic oscillation. The rigid wall created asymmetry in the flow field and forced the bubble to collapse non-spherically,

so that a jet pointing from high pressure to low pressure was generated and penetrated the opposite edge of the bubble. With the development of high-speed photography, the dynamic behaviors of cavitation have been deeply studied under the constraint conditions of a solid wall,[15–17] an elastic boundary,[18–20] a free surface,[21–23] and body force.[24,25] Supponen et al.[26] classified the jets into three distinct regimes: weak, intermediate, and strong, combining theoretical considerations with hundreds of high-speed visualizations of bubbles collapsing near different kinds of boundaries.

For the surrounding boundaries, the dynamic behaviors of cavitation in a narrow tube have attracted more and more attention and are of significance in various applications such as underwater propulsion,[27,28] fluid mixing and pumping in microfluidic devices,[29,30] and needle-free injection applications.[31,32] In this

background, scholars devoted various experimental and numerical works to gain a better understanding of the dynamic behaviors of bubble pulsation in the tube. Ory et al.[33] studied the fluid dynamics of the growth and collapse of a vapor bubble in a small tube. It was found that the curvature of the end surfaces of the bubble during collapse remained relatively small. Sun et al.[34] analyzed the length and volume of a laser-induced cavitation bubble in a microtube. The experimental observation showed that the cavitation bubble expanded and contracted along the microtube. These studies indicate that the bubble motion in the tube can remain very nearly one-dimensional until the end of the collapse. On the other hand, Xu et al.[35] investigated the dynamic characteristics of a spark-induced cavitation in a rigid tube using high-speed observation. The length and the inner diameter of the tube were 112 mm and 8 mm, respectively. At the stage of contraction, the bubble was deformed into toroidal since an axial jet pierced its surface. After the collapse of the toroidal bubble, a swirling jet pointing toward the circumferential wall of the tube was generated. The generation of the swirling jet is suggested to be because of three-dimensional collapse in the study of the bubble dynamics. Similar phenomena were also observed in the studies of Ji and Zou et al.,[36,37] Ni et al.,[38] Zhang et al.,[39] and Wang et al.[40] Besides, Ji et al.[37] also observed a phenomenon of secondary cavitation when the spark-induced cavitation collapses in the tube. From the studies mentioned above, it is worth noting that the bubble motion shows apparent differences during its growth and collapse because of the flow state in tubes with different sizes. Thus, it is required to analyze the dimensional effects of the bubble's motion and the transition mechanism of different pulsation patterns.

From these backgrounds, it is interesting to investigate the dynamic behaviors of bubble motion in a tube. In the experiment, a Nd:YAG laser is used to generate cavitation bubbles in an acrylic tube. A high-speed observation is carried out to investigate the pulsation of the cavitation bubble with different length-to-diameter ratios. To clarify detailed information like the interface instability and flow field, numerical simulations based on the volume-of-fluid (VOF) method are also implemented on the open source code Open-FOAM in consideration of the liquid compressibility and accurate capture of the phase interface. From the experimental observation and numerical analysis, the dimensional effects of the bubble motion are related to the type of the generated axial jet pointing toward the tube's end. For the first pulsation period, we investigate three different regimes of collapse patterns. Finally, the transition mechanism of the bubble pulsation from one dimension to three dimension is discussed by combining with some other experimental results.

II. EXPERIMENTAL SETUP

The experimental apparatus for the observation of a laser-induced cavitation in a tube is shown in Fig. 1. An acrylic-made tube with the outer diameter of 20 mm is fixed by a holder in a water tank containing distilled water and the tube's inner diameter is varied under different conditions. The size of the water tank is 100 mm in width, 300 mm in length, and 100 mm in depth. The cavitation is generated by focusing a Nd:YAG laser pulse (Quanta-Ray Pro, Spectra-Physics, CA, USA) on a black point on the front end, which is blocked by a thin acrylic slice. The wavelength of the laser pulse is 1064 nm, the duration of the laser is 10 ns, and the spot area on the front end of the tube is about 0.785 mm^2. The laser energy is measured by an energy meter (Vega, Ophir Optronics Solutions Ltd., Jerusalem, Israel). To better observe the morphology and other characteristics of the cavitation bubble, an experimental visualization is carried out using a high-speed camera (Phantom V1612,
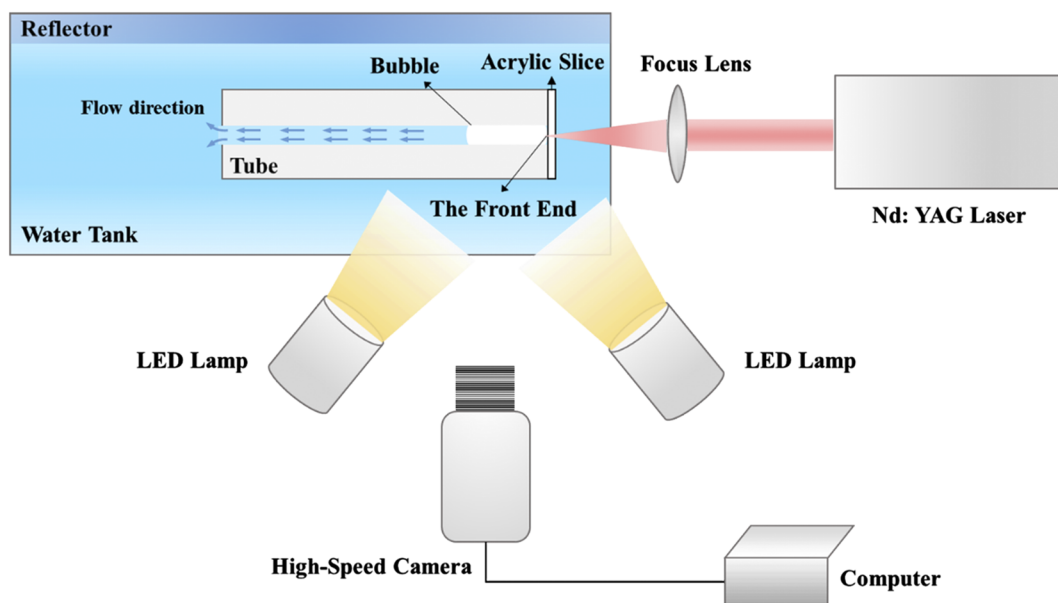

FIG. 1. Experimental arrangements for the observation of a laser-induced bubble in a tube.

Vision Research, NJ, USA), a macro lens (MP-E 65 mm, Canon, Inc., Tokyo, Japan), and two bright light emitting diode (LED) lamps (CLL-4800TDX, Falcon Eyes Ltd., Shenzhen, China) with a color temperature of 6000 K. As shown in Fig. 1, the light is reflected into the camera through a reflector placed opposite in tank to meet the amount of light entering at a high shooting speed.

III. NUMERICAL METHOD

For the numerical simulation of the dynamic behaviors of cavitation bubbles, the boundary element method,[38,41] the VOF method,[42,43] and the level-set method[44,45] are commonly used to analyze the phase interface. Besides, it is required to consider the compressibility and immiscibility of the fluid for describing the bubble morphology and reveal some key scientific problems, such as the mechanism of jet formation and the interface instability based on previous studies.[46,47] Therefore, to better understand the detailed information of the surrounding flow field around the bubble and to reveal the jet mechanism during bubble shrinkage and collapse in the presence of interface instability, the VOF method is implemented on the open source computational fluid dynamics (CFD) platform OpenFOAM[48] and the compressible multiphase solver *compressibleInterFoam* is used in the simulation. The solver uses MULES algorithm to maintain a sharp interface between two phases and it is based on the flux-corrected transport (FCT) method, which is an algebraic reconstruction method of the interface. In the VOF method, a variable α is defined to represent the phase fraction of the fluid. Here, $\alpha = 1$ and $\alpha = 0$ mean that the grid is full of liquid and gas, respectively. The governing equations and settings of the physical constants involved in the simulation are listed in Appendix A. All partial differential equations in the solver are solved using the finite volume method.

To investigate the dimensional effects of the bubble pulsation in a tube, simulations are carried out in three-dimensional geometry. The o-block structured grid method is used in meshing, a tube with the size of 40 mm in length and 3 mm in inner diameter is chosen as an example to illustrate the mesh situation as shown in Fig. 2. According to the experimental setup, the cavity with high pressure and temperature is set on the front end of the tube and the pulsation of the bubble is within the region A. The grids in region A are adequately refined to capture the flow field accurately. A cube of $10 \times 10 \times 10$ mm³ is placed in region B to simulate the fluid area outside of the tube and reduce the impact and reflection of the pressure wave. The boundary conditions are set as follows: the pressure of the cube's top surface (the yellow part of Fig. 2) is set to a fixed value of 101 325 Pa, and the phase fraction is set to a fixed value as one since the tube is immersed entirely in the water. The other boundaries are set to no-slip boundary conditions.

To establish the accuracy of the CFD solution and to maintain a high computational efficiency, the medium mesh with approximately one million grids is selected to simulate the bubble pulsation in a tube based on the grid convergence study in Appendix B.

IV. RESULTS AND DISCUSSION

A. Typical observations of bubble dynamic behaviors in a tube

Figure 3 shows the images of the pulsation of a laser-induced cavitation in a tube. The high-speed camera captures the images at a frame rate of 40 kfps and an exposure time of 3 µs. In the experiment, the energy of the laser pulse is about 0.958 J. The tube with a length of 40 mm and an inner diameter of 3 mm is immersed in the water tank full of distilled water. The strong flash is captured in Fig. 3(a) and indicates the generation of the laser-induced plasma. Based on the previous studies,[49] the duration of the plasma flash is approximately 200 ns. Here, first compression waves can be generated by the expansion of the plasma channel although they cannot be captured in the figure. Subsequently, the bubble begins to expand driven by the pressure gradient. A group of small bubbles is observed on the wall of the tube from approximately 0.9 ms [Fig. 3(d)]. These small bubbles expand and shrink along the tube axis during the cavitation expansion. This phenomenon is also called the secondary cavitation, which was found in the Ji's experiment[37] as well. The secondary cavitation can be induced due to the tensile area behind the reflection of the first compression waves. At 2.4 ms, the bubble surface in the middle seems to stop expanding, while the part close to the tube wall continues moving forward with the bubble expansion. Thus, the concave shape at the bubble surface is formed. The bubble reaches the maximum length of 11.12 mm at 2.9 ms. It should be noted that there are small chaotic bubbles that appear and develop accompanied by the main bubble during the expansion [Figs. 3(e)–3(h)],
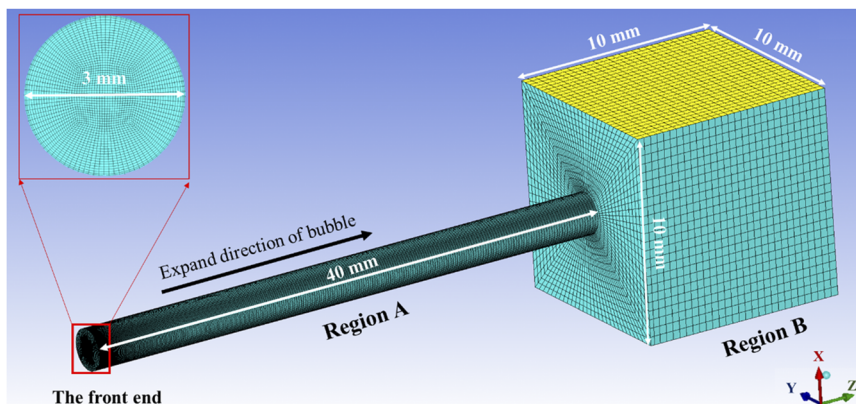

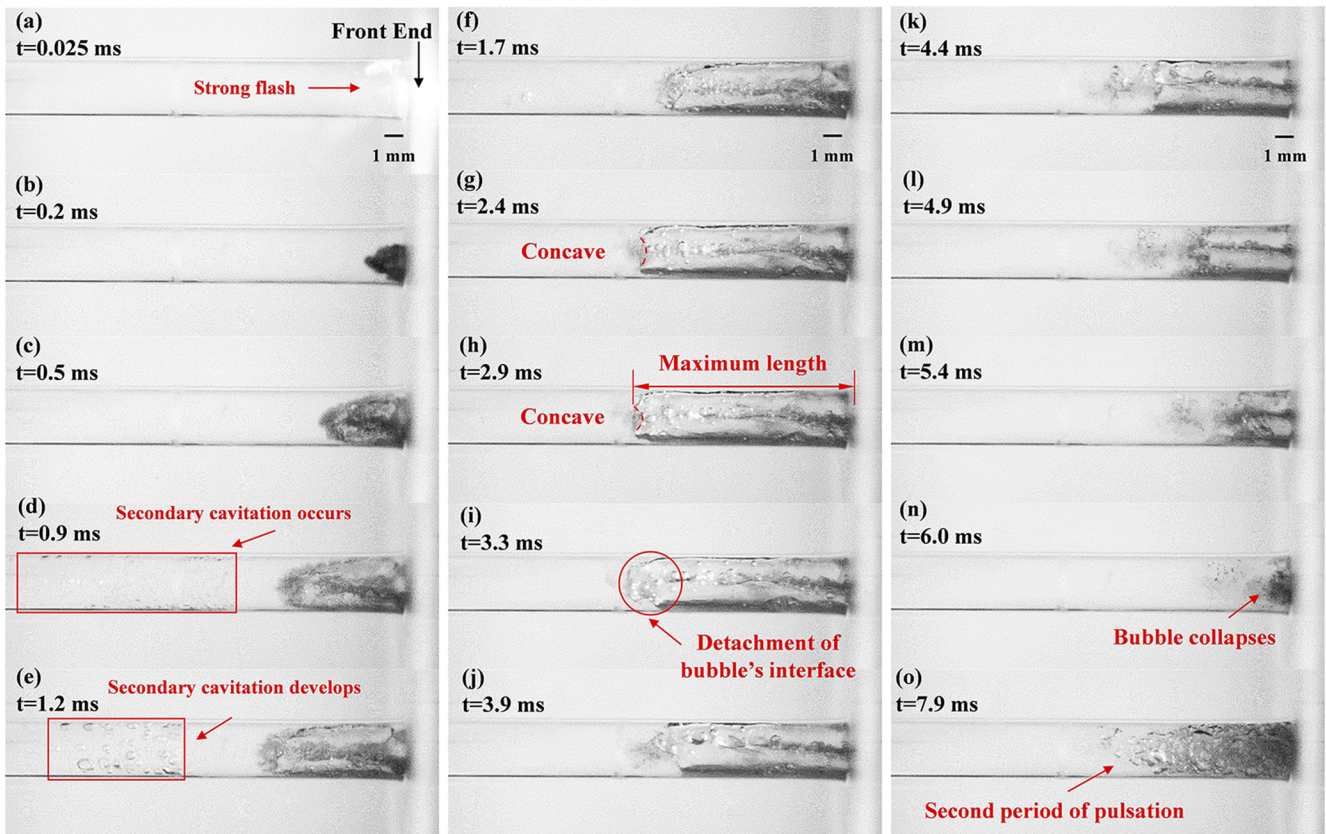**FIG. 2**. Simulation geometry and mesh situation.

FIG. 3. Experimental temporal variation of a laser-induced bubble pulsation in the tube: D = 3 mm and L = 40 mm. (a) Cavitation appears; [(b)–(h)] bubble expands; [(i)–(n)] bubble contracts; and (o) the rebound of the bubble.

while they weakly affect the morphology of the main bubble. These bubbles may be caused by the focusing method of the laser since we smear the black ink in the front of the tube to gather the energy of the laser easier. With the shrinkage of the cavitation, a detachment phenomenon occurs at the concaved part of the bubble, at 3.3 ms. The detachment can be caused by the shear flow due to the wall effect. At last, it collapses at t = 6.0 ms in Fig. 3(n). After that, many small and chaotic bubbles are formed during the rebound period, as shown in Fig. 3(o). In general, these bubbles pulsate several similar periods under the pressure difference although the pulsation amplitude decreases gradually until the oscillation disappears. The results suggest that the pulsation of the laser-induced cavitation barely have quantitative characteristics after the first collapse. Hence, the bubble motion during the first period is our main concern in the present study. The maximum length and pulsation period of the bubble are thought to be used to describe the characteristics of the bubble pulsation. Compared with the previous observation,[34] the pulsation of the bubble in this case seems not to remain one-dimensional since the surface of the bubble is no longer flat during bubble pulsates.

Based on the experimental condition in Fig. 3, a numerical simulation is carried out and the results are shown in Fig. 4. For simulating a laser-induced cavity, setting the initial conditions is challenging. The empirical formula and a theoretical model are commonly used to determine the initial conditions, such as the Rayleigh–Plesset equation used in the infinite liquid. According to other discussions on the bubble evolution in a fluid,[21,38,43,47,50,51] the laser-induced cavitation can be initiated by setting a small volume of high-pressure gas. In the present study, a quasi-one-dimensional model [Eq. (1)] of the bubble pulsation in a tube[34,52] is used to determine the pressure inside the initial bubble in the numerical simulation,

$$l_L \rho_L \frac{d^2 X}{dt^2} = P_b(t) - P_\infty - \xi \frac{dX}{dt}. \tag{1}$$

Here, l_L is the length of the liquid column inside the tube, ρ_L is the liquid density, X is the length of the bubble, $P_b(t)$ is the time-varying pressure inside the bubble, P_∞ is the ambient pressure, and ξ represents the effect of viscous losses due to the tube's wall, and it can be modeled as $\xi = 32 \mu_L l_L / D^2$; here, μ_L is the liquid dynamic viscosity and D is the diameter of the tube. Assuming there is no heat transfer between liquid and gas, Eq. (1) can be derived as

$$l_L \rho_L \frac{d^2 X}{dt^2} = P_0 \left(\frac{V_0}{V(t)} \right)^\gamma - P_\infty - \xi \frac{dX}{dt}, \tag{2}$$
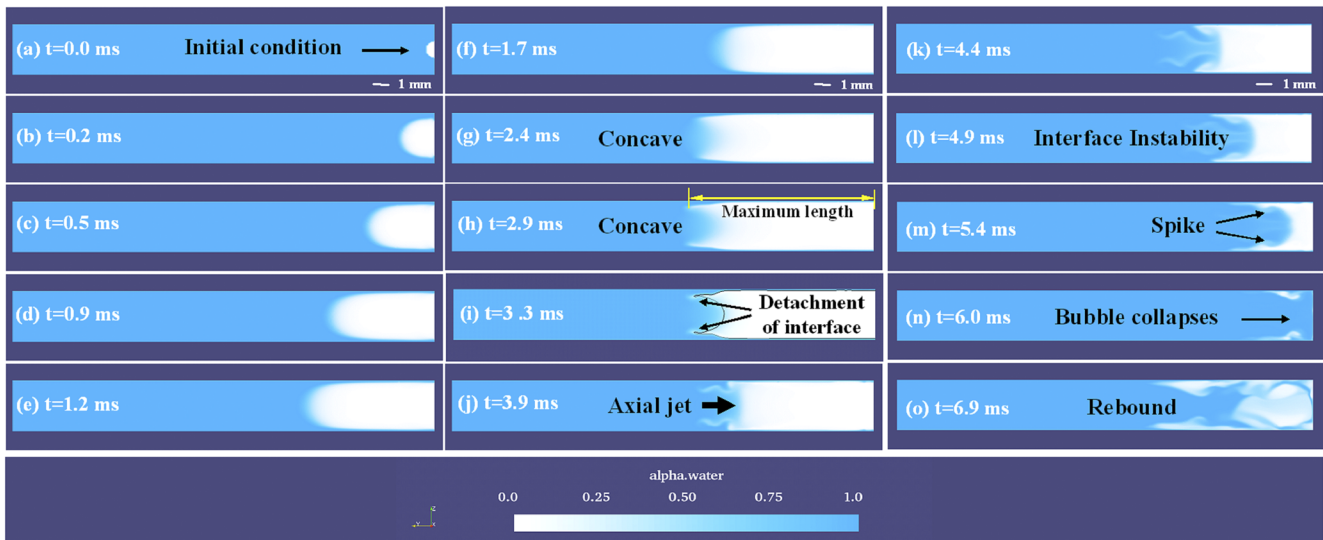
FIG. 4. Numerical simulation results of temporal variation of bubble pulsation in a tube: (a) initial condition; [(b)–(h)] bubble expands; [(i)–(n)] bubble contracts; and (o) the rebound of the bubble. The view is a $x = 0$ slice along the diameter of the tube. The alpha.water is the volume fraction of the water phase: 0 represents pure gas and 1 represents pure water. The black line in (i) represents the contour of the phase fraction of 0.5.

where P_0 is the pressure of the initial bubble, V_0 is the volume of the initial bubble, $V(t)$ is the time-varying volume of the bubble, and γ is the polytropic exponent. Thus, the pressure of the initial bubble can be determined by solving Eq. (2) combining with the experimental conditions. In the typical case, the size of the tube is 40 mm in length and 3 mm in inner diameter. The initial radius of the cavity is determined by the spot area of the laser on the bottom of the tube. Hence, $l_L = 40 - x$, $\rho_L = 998$ kg/m^3, $P_\infty = 101\,325$ Pa, $\mu_L = 1.004 \times 10^{-3}$ kg/m^3, $V_0 = 0.262$ mm^3, and $\gamma = 1.4$. By solving Eq. (2), the initial pressure inside the cavity is 9.3 MPa. In addition, the temperature of the initial bubble is set as 900 K, based on the experimental results and thermodynamic analysis of laser-induced bubbles.[53–55] Comparing the experimental observation in Fig. 4 with the numerical results in Fig. 5, it is reasonable to describe the bubble dynamics for the setting method of the initial condition inside the cavity.

As for the simulation results of the typical case, Fig. 4 describes the behaviors of the bubble motion at the section ($x = 0$) along the central axis of the tube. As shown in Figs. 4(a)–4(f), we can see that the appearance of the bubble remains very nearly one-dimensional. However, from the later stage of the expansion, the front interface of the bubble is deformed into a curved shape, changing from the convex shape to the concave shape [Fig. 4(g)]. Next, the detachment phenomenon occurs equally at the concave part of the bubble. From Fig. 4(j), an axial jet is formed and moves toward the tube's front end. From the shape of the bubble surface, it is found that the interface instability happens at the later stage of the shrinkage [Fig. 4(l)]. The shape of "spike," a classical phenomenon in the Rayleigh–Taylor (RT) instability forms at the interface [Fig. 4(m)]. After the axial jet penetrates the bubble wall, the main bubble collapses at about 6.0 ms. According to the studies by Ni et al.[38] and Aghdam et al.,[56] it is suggested that the bubble cannot remain nearly

one-dimensional during the collapse in this case. In addition, the group of small bubbles in Fig. 3(e) does not occur in the simulation because the phase transition process cannot occur when the local pressure drops below the saturated vapor pressure or gas nuclei develop into bubbles.

For the first cycle, the comparison of the experimental data and numerical results of bubble pulsation is shown in Fig. 5. The bubble length is measured based on the experimental and numerical images, using the distance between the front edge of the bubble and the end of the tube as a standard. The central difference scheme is utilized
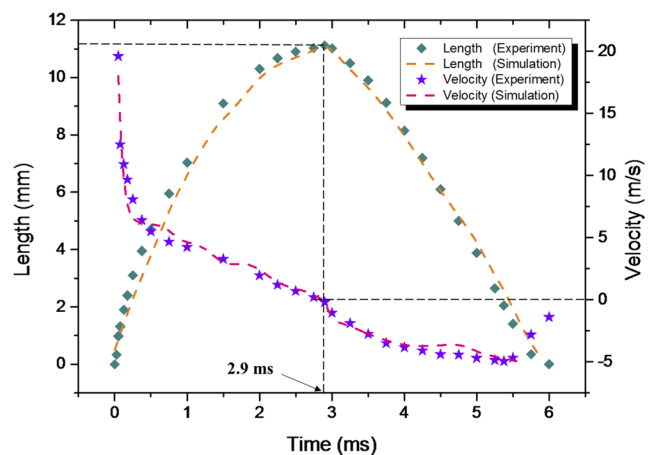

FIG. 5. Comparisons of the bubble length and surface velocity between experimental observation and numerical results. The axial direction of expansion is positive.

to calculate the velocity of the front surface of the bubble. The solid squares and stars are the length and velocity of the bubble obtained by the experimental observation, respectively. The dashed lines represent the numerical results. From the experimental results, it is found that the initial velocity of the bubble's front surface reaches about 11 m/s due to a large pressure difference between inside and outside the cavity. During the early stage of the expansion, the velocity decreases remarkably and gradually until the bubble nearly contracts to a minimal size. Subsequently, the surface velocity begins to increase around the bubble collapse. It indicates that the acceleration at the bubble surface points toward the liquid phase from the gas phase during this period. Consequently, the bubble interface is very unstable around the collapse owing to the RT instability, as shown in Figs. 4(l)–4(n). Generally speaking, the numerical results agree well with the experimental results during the first pulsating period, including the bubble's length and pulsating period. It is reasonable to use the numerical method for describing the bubble pulsation in the tube.

B. Effects of the controlling parameters on bubble dynamics

Next, we discuss the dynamics of the bubble under different initial conditions. When ignoring gravity, mass exchange, and heat transfer between the bubble and liquid, the main parameters affecting the pulsation of the bubble are the energy of the bubble and length-to-diameter ratio of the tube in the present study. First is the effect of the initial energy of the bubble. According to the study by Vogel et al.,[57] only a small part of the laser energy is used to nucleate the cavitation bubble. Hence, an appropriate energy scale is the work done to form a cavity of a certain volume against the ambient pressure, e.g., $J \approx P_{\infty} V_m$. The P_{∞} is the ambient pressure and V_m is the maximum volume of the cavity. Hence, the normalized initial energy of the bubble is shown as follows:

$$J^* = \frac{J}{P_{\infty} V_{ref}}, \quad (3)$$

where V_{ref} is the reference volume, which is the volume of the tube, $V_{ref} = \pi D^2 L/4$. Here, L is the length of tube and D is the diameter of tube.

In the experiments, the initial energy of the bubble is altered by changing the laser energy. Figure 6 shows the experimental results of the bubble's length at a different energy of the laser. The solid squares, triangles, diamonds, and stars are the experimental results at the laser energies of 0.991 J, 1.373 J, 1.624 J, and 1.921 J, respectively. From the figure, it is found that the surface velocity of the bubble increases with the increasing energy of the laser, so that the maximal length and the pulsation period of the bubble increase. The maximal lengths of the cavitation are 12.88 mm, 16.33 mm, 17.61 mm, and 18.90 mm as energies increase. From these results, the average of conversion factor between the laser energy and the bubble energy is about 1% in the present study. Hence, the normalized energies of the cavitation bubble are obtained to be 0.322, 0.408, 0.440, and 0.473, respectively. The corresponding pulsation periods are 6.125 ms, 6.625 ms, 6.750 ms, and 6.875 ms, respectively.

According to the results in Fig. 6, the relationships between the dynamic behaviors and the energy of the bubble are obtained
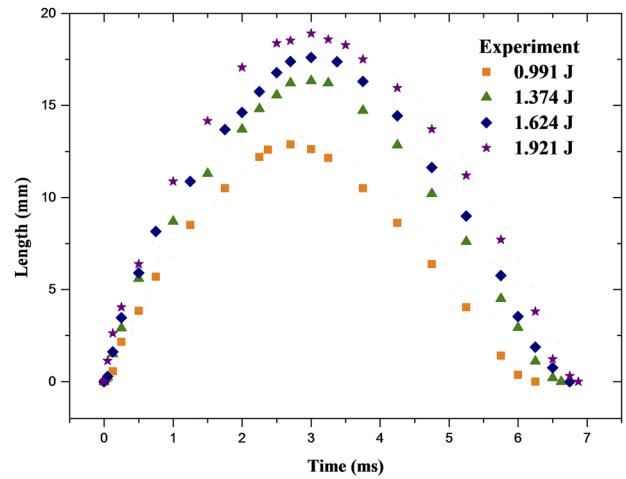
FIG. 6. Estimation of the length of the bubble at laser energies of 0.991 J, 1.373 J, 1.624 J, and 1.921 J.

in Fig. 7. The abscissa is the normalized energy J^*. The ordinates are the normalized maximum length X_m^*, which is defined as

$$X_m^* = X_m/D, \quad (4)$$

and the normalized first pulsating period τ^* is defined as

$$\tau^* = \frac{t}{D} \sqrt{(P_{\infty} - P_v)/\rho_l}. \quad (5)$$

The solid circles and stars represent the maximal length and the pulsating period, respectively. Linear fitting lines are also added in the figure. The coefficients of the Pearson correlation are 0.994 between J^* and X_m^* and 0.993 between J^* and τ^*. The results show
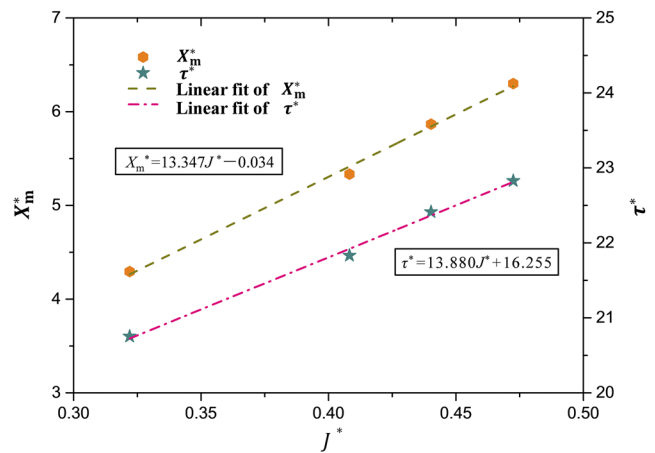
FIG. 7. The relationships between the normalized initial energy and the dynamic behaviors of the bubble: blue star: the pulsating period and orange hexagon: the maximum length of the bubble. Linear fit of J^* and X_m^*: Pearson correlation coefficient = 0.994 and linear fit of J^* and τ^*: Pearson correlation coefficient = 0.993.
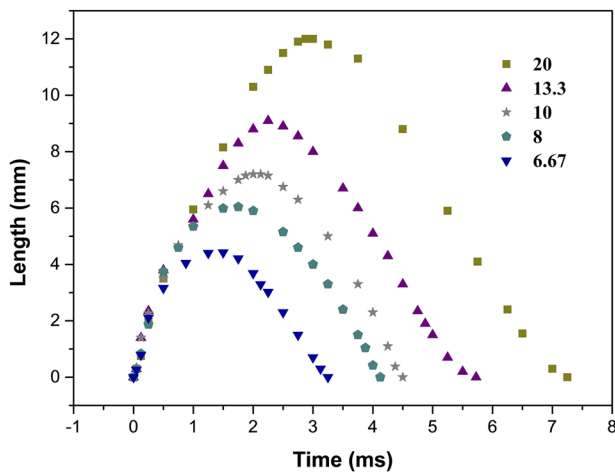
FIG. 8. The time history of bubble lengths at different length-to-diameter ratios of 20, 13.3, 10, 8, and 6.67.
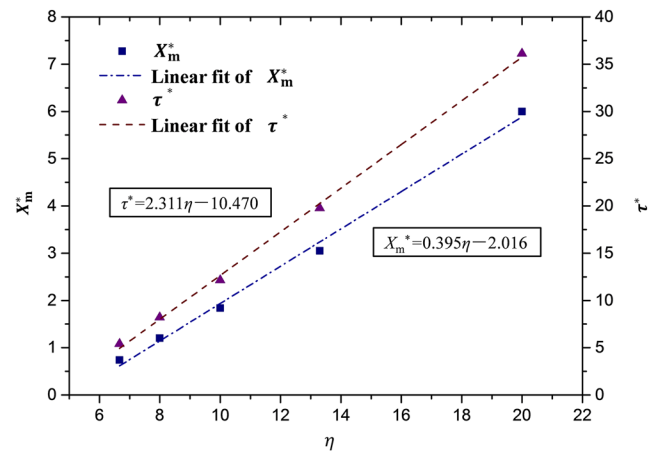

FIG. 9. The relationships between normalized length-to-diameter ratios of the tube and the bubble pulsation: purple triangle: the pulsating period and blue square: the maximal length of the bubble. Linear fit of X_m^*: Pearson correlation coefficient = 0.998 and linear fit of τ^*: Pearson correlation coefficient = 0.999.

that both the maximal length and the pulsating period have good linear correlations with the energy of the cavitation, respectively. However, the linear relationship is applicable in the interval which is displayed in Fig. 7, the relationship may change for a much higher or lower J^*.

The experimental observation is also carried out using tubes with different length-to-diameter ratios. The results are shown in Fig. 8. The length-to-diameter ratio of the tube η is described as

$$\eta = L/D. \tag{6}$$

In the experiments, the tube's length is set as 40 mm and the inner diameters of the tube are 2 mm, 3 mm, 4 mm, 5 mm, and 6 mm for length-to-diameter ratios of 20, 13.3, 10, 8, and 6.67, respectively. The energy of the laser is 0.705 J. From the figure, the surface velocities are almost the same during the expansion of the bubble. For a tube with a large length-to-diameter ratio, the bubble has a larger maximal length and longer pulsating period. The maximal lengths are 12 mm, 9.15 mm, 7.35 mm, 6.01 mm, and 4.43 mm for the length-to-diameter ratios of 20, 13.3, 10, 8, and 6.67. The corresponding pulsating periods are 7.5 ms, 5.95 ms, 4.875 ms, 4.125 ms, and 3.25 ms, respectively. Based on these results, relationships between the bubble pulsation and the tube sizes are obtained in Fig. 9. The abscissa is the length-to-diameter ratio; the ordinates are the normalized maximum length and the normalized first pulsating period, respectively. The solid triangles and squares represent the experimental results of the maximal length and the pulsating period, respectively. The coefficients of the Pearson correlation are 0.998 between η and X_m^* and 0.999 between η and τ^*. The results show that the dimensionless maximum length and the dimensionless first period increase linearly with the length-to-diameter ratio.

C. Dimensional effects of bubble pulsation in a tube

For the bubble collapsing near a rigid surface, near a free surface, or in variable gravity, Supponen et al.[26] classified the jet

into three distinct regimes: weak, intermediate, and strong. The weak jets hardly penetrate the bubble surface and remain within it through the collapse and rebound. The bubble is thought to remain spherical despite the jet generation. For the intermediate jets, they pierce the bubble surface just before the collapse. The strong jets penetrated the bubble surface early during the collapse. However, we also found the similar phenomena when investigating the bubble dynamics in a tube. Combining the experimental observation with the numerical simulation, it is found that the type of the generated jet is closely related to the collapse patterns of the bubble motion. The collapse patterns include one-dimensional effect, transitional effect, and three-dimensional effect. The three typical cases of three collapse patterns in the tube are shown in Fig. 10. The velocity field around the bubble is also presented in the figure to understand the pulsation of the bubble better. The moment of (a) describes the shrinkage of the bubble. At the moment of (b), the jet reaches the front end of the tube. The (c) represents the collapse of the bubble. The moment of (d) is the bubble rebound.

First is the one-dimensional effect. As described in Fig. 10(1), the bubble interface remains uniform and continuous during its growth and collapse. The normalized energy of the bubble and length-to-diameter ratio of the tube are 0.363 and 13.3, respectively. At the moment of (c), we found that the whole flow field points toward the front end of the tube. However, it is worth noticing that the bubble motion also remains one-dimensional when a generated weak jet always exist within the bubble, referring to the study by Supponen et al.[26] The intermediate jet corresponds to the bubble motion in the transition regime between one dimension and three dimensions, as shown in Fig. 10(2). The normalized energy of the bubble and length-to-diameter ratio of the tube are 0.265 and 8, respectively. At the moment of (a), the shape of the interface looks like "spike," a classical phenomenon occurring in the RT instability. After the axial jet penetrates the bubble wall, the collapse of the main bubble occurs. At this moment, it is

(1) the one-dimensional effect situation (J^*=0.363, $\eta = 13.3$)
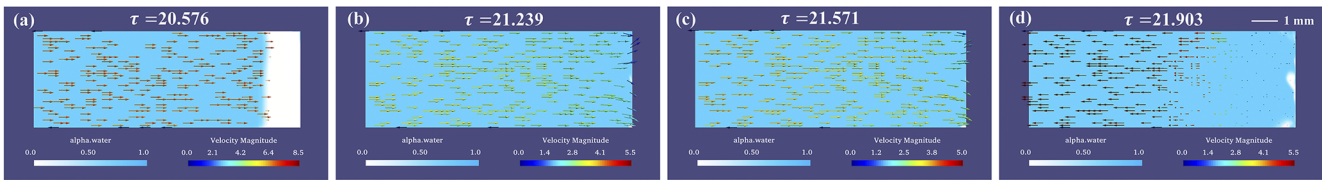
(2) the transition situation (J^*=0.265, $\eta = 8$)
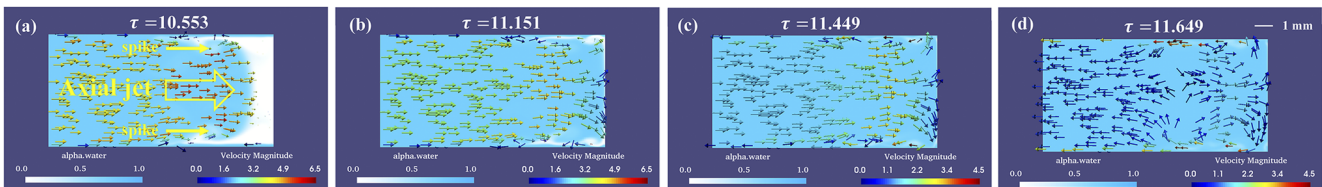
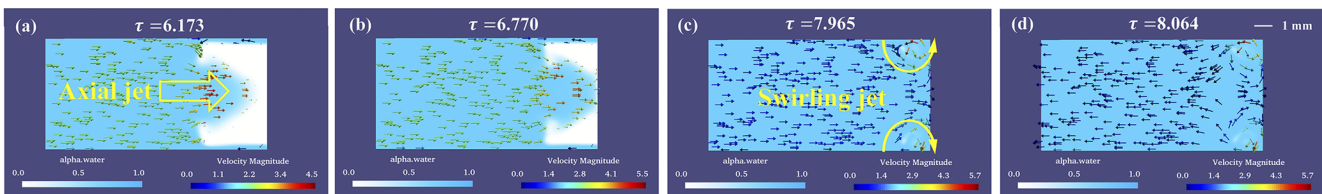**(3) the three-dimensional effect situation (J^*=0.127, $\eta = 8$)**

FIG. 10. Simulation of typical cases about three collapse patterns of the bubble motion in the tube: (1) one-dimensional effect, (2) transition effect, and (3) three-dimensional effect. The results are the sectional view ($x = 0$) along the diameter of the tube, and the arrow indicates the direction of the velocity vector on the section.

found that the flow near the tube's end moves toward the circumferential wall of the tube compared with that of one-dimensional effect. Figure 10(3) shows a case of the three-dimensional effect. The normalized energy of the bubble and length-to-diameter ratio of the tube are 0.127 and 8, respectively. As shown at the moment of (b), the toroidal bubble is formed. This phenomenon is commonly observed in the cases of the strong jets referring to the studies.[35,38,39,56] In this case, the strong axial jet generally penetrates the opposite bubble wall during the early stage of the shrinkages, Hence, the toroidal bubble is remarkably forced to collapse, so that the swirling jets pointing toward the tube wall is generated at the collapse, as shown in the distribution of the flow field at the moment of (c). As a result, the collapse patterns of the bubble pulsation in a tube are determined by the types of the axial jet, and the swirling jets can be used as a basis for discriminating the three-dimensional effect. We can conclude from the above discussion that the normalized energy of the bubble and the length-to-diameter ratio are main factors in affecting the dimensional characteristics of the bubble.

Combining the experimental observation with the numerical simulation, a summary of the bubble pulsation in the tube is presented in Fig. 11. The abscissa is the normalized energy of the initial cavity and the ordinate is the normalized length-to-diameter ratio of the tube. The three regimes of bubble pulsation in a tube are plotted with distinct symbols. The circles, stars, and triangles represent the results of one-dimensional effect, transitional effect, and three-dimensional effect, respectively. The open and solid symbols are the numerical and experimental results obtained from the present

study, respectively. The pink solid symbols indicate the experimental observation by Ni et al.[38] As expected, the high-energy, thin-tube regime is dominated by the one-dimensional effect. While keeping the length-to-diameter ratio constant, we secondly observe the transition regime. In this regime, the RT instability occurs obviously at the bubble interface before the generated axial jet penetrates the bubble wall, but a swirling jet pointing the tube wall is
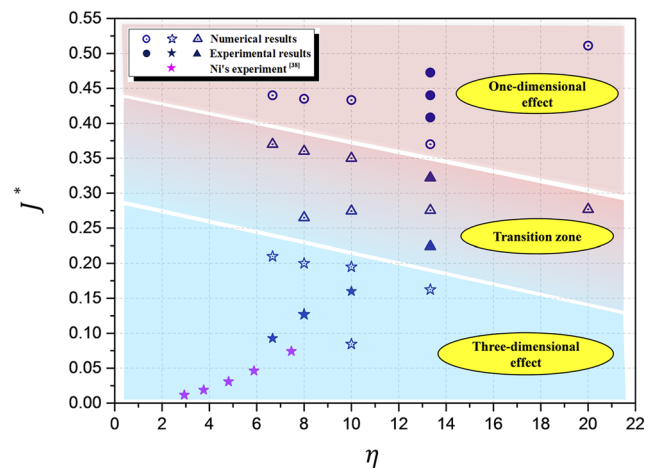

FIG. 11. Phase diagram of the dimensional effect of collapse patterns.

not induced. Subsequently, the three-dimensional effect dominates the low-energy, thick-tube region. After the axial jet pierces the bubble surface, a swirling jet is generated during the collapse. But the RT instability is not clearly observed. However, there is a special observation in this case. It is that the bubble cannot occupy the whole diameter of the tube during its growth and collapse. In addition, two lines are added among the three regimes. Besides possible boundaries of each regime, the slopes of two lines indicate that the one-dimensional effect becomes dominant with increasing length-to-diameter ratios of the tube. It should be noted that, in this phase diagram, the Reynolds number (Re) representing the ratio of inertial force to viscous force and the Ohnesorge number (Oh) relating the viscous forces to inertial and surface tension forces vary as well when the normalized energy and the length-to-diameter ratio are changed. Moreover, we should also notice that the phase diagram is obtained for the bubble collapse in water, and therefore, the area of the three regimes is changed for other liquid media since the physical properties of the liquid medium affect Re and Oh as well.

V. CONCLUSION

In this study, the dynamic behaviors of a laser-induced bubble in a tube are analyzed experimentally and numerically. A high-speed optical visualization was carried out to observe the physical processes of the bubble under different initial conditions. The numerical simulation based on the VOF method was also implemented on the open source code OpenFOAM. From the experimental observation and simulation results, an axial jet was generated and it penetrated the opposite surface of the bubble at the end of the shrinkage and collapse, which leads to different collapse patterns. In the meantime, RT instability can occur at the bubble interface around the collapse. It suggests that the maximum length and pulsation period of the bubble are used to describe the bubble pulsation. We analyzed the effects of the initial energy of the cavitation and length-to-diameter ratio of the tube on dynamic behaviors of the bubble. The experimental results show that the bubble motion had linear correlations with the initial energy of the bubble and length-to-diameter ratio of the tube. Here, the conversion factor between the laser energy and the bubble energy was about 1% for the present experimental setup.

According to the type of the axial jet, the collapse patterns during the first pulsation of the bubble were classified into three regimes: one-dimensional, transitional, and three-dimensional. In the regime of the one-dimensional effect, the interface of the bubble remained uniform and continuous during growth and collapse. The flow field pointed toward the front end of the tube uniformly. For the bubble motion in the transition regime, the RT instability was obviously observed at the bubble's interface before the axial jet penetrated the opposite surface of the bubble. After the bubble collapsed, the flow around the bubble moved toward the circumferential wall of the tube. Compared with the case in the transition regime, a toroidal bubble was formed after the axial jet penetrated the bubble. Furthermore, swirling jets pointing toward the tube's circumferential wall were formed during the bubble collapse in the regime of the three-dimensional effect. Finally, a phase diagram discriminating the collapse patterns was obtained. The one-dimensional effect becomes dominant with increasing length-to-diameter ratio of the

tube. These new findings in the present study are helpful for understanding clearly bubble dynamics under the constrained conditions and may provide theoretical support for engineering applications. For better comprehension of the effect of Re and Oh, it may be interesting to investigate the collapse patterns of bubble pulsation in a tube for different liquid media.

DATA AVAILABILITY

The data that support the findings of this study are available from the corresponding author upon reasonable request.

APPENDIX A: GOVERNING EQUATIONS AND SOLUTION ALGORITHM OF THE COMPRESSIBLE-INTERFOAM

In the numerical simulation, the VOF method is used to investigate the pulsation of the cavitation in the tube based on the open source computational fluid dynamics (CFD) platform OpenFOAM. The governing equations consist of the continuity equation, momentum equation, energy equation, and the transport equation of the phase fraction. The two phases are assumed to be homogeneous. The continuity equation is given as

$$\frac{\partial \rho}{\partial t} + \nabla \cdot (\rho \mathbf{U}) = 0, \tag{A1}$$

where ∇ is the gradient operator, $\mathbf{U}$ is the velocity vector, ρ is the mixture density and defined as

$$\rho = \rho_{\text{liquid}}\alpha + \rho_{\text{gas}}(1 - \alpha). \tag{A2}$$

The momentum equation is given as

$$\frac{\partial}{\partial t}(\rho \mathbf{U}) + \nabla \cdot (\rho \mathbf{U}\mathbf{U}) = -\nabla\left(p + \frac{2}{3}\mu\nabla \cdot \mathbf{U}\right) + \nabla \cdot \left(\mu\left(\nabla \mathbf{U} + (\nabla \mathbf{U})^{\text{T}}\right)\right)$$
$$+ \rho g + \sigma\kappa\nabla\alpha, \tag{A3}$$

where p is pressure, μ is the dynamic viscosity of the mixture of two phases, $\mu = \mu_{\text{liquid}}\alpha + \mu_{\text{gas}}(1 - \alpha)$, g is the gravitational acceleration, σ is the surface tension coefficient, and κ is the curvature of the interface, $\kappa = \nabla \cdot (\nabla\alpha/|\nabla\alpha|)$.

The energy equation is given as

$$\frac{\partial \rho T}{\partial t} + \nabla \cdot (\rho \mathbf{U}T) - \nabla \cdot (\mu T) = -\left(\frac{\alpha}{C_{\text{v.liquid}}} + \frac{1 - \alpha}{C_{\text{v.gas}}}\right)$$
$$\times \left(\frac{\partial \rho k}{\partial t} + \nabla \cdot (\rho \mathbf{U}k) + \nabla \cdot (p\mathbf{U})\right), \tag{A4}$$

where T is the temperature, $C_{\text{v.liquid}}$ and $C_{\text{v.gas}}$ are the heat capacities of liquid and gas phases, respectively, and k is the kinetic energy per unit mass, $k = |\mathbf{U}|^2/2$.
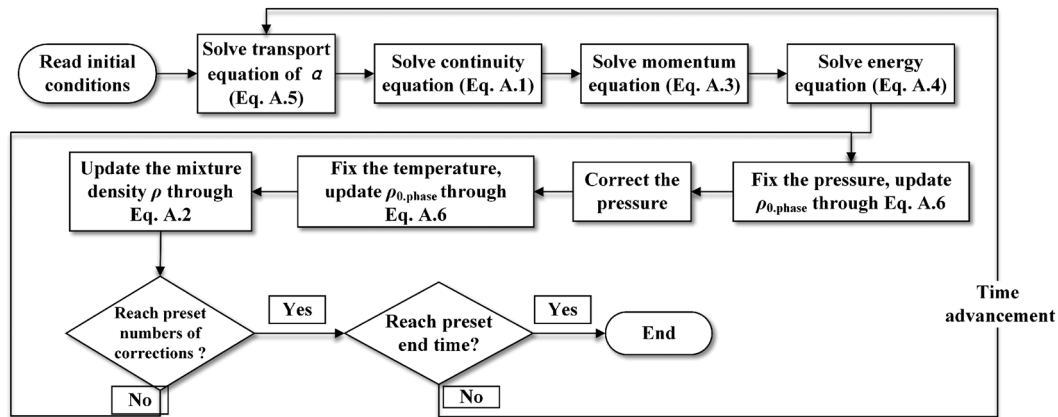
FIG. 12. The flow chart of the solution algorithm in the compressibleInterFoam.

To consider the compressibility and immiscibility of the fluid, the multiphase solver compressibleInterFoam is used in the present study. The MULES algorithm is applied to maintain a sharp interface between the two phases. The transport equation of the phase fraction is

$$\frac{\partial \alpha}{\partial t} + \nabla \cdot (\alpha \mathbf{U}) + \nabla \cdot (\alpha(1-\alpha)\mathbf{U}_r) = 0, \quad (A5)$$

where the relative velocity $\mathbf{U}_r$ is defined as $\mathbf{U}_r = c_\alpha |\mathbf{U}| \nabla \alpha / |\alpha|$ and c_α is the artificial compressive coefficient. The third term in Eq. (A5) is an artificial compression term which is utilized to sharpen the interface of two phases.

Finally, the equation of the state for two phases is given by

$$\rho_{\text{phase}} = \rho_{0.\text{phase}} + \psi(p - p_{0.\text{phase}}), \quad (A6)$$

where $\rho_{0.\text{phase}}$ and $p_{0.\text{phase}}$ are the initial density and pressure of one specific phase, and ψ is the compressible coefficient, $\psi = 1/c^2$, c is the speed of sound. For the gas phase, $\rho_{0.\text{phase}}$ and $p_{0.\text{phase}}$ are set to zero, e.g., it obeys the ideal gas state equation.

The PISO algorithm[58] is integrated in the solver to solve this transient flow problem. The flow chart of this method for solving the governing equations is shown in Fig. 12. All the partial differential equations are solved based on the finite volume method.

The physical constants involved in the simulation are set as Table I shows.

TABLE I. Settings of the physical constants involved in the simulation.

Phase	$\rho_{0.\text{phase}}$ (kg/m^3)	μ (kg/m^3)	g (m/s^2)	σ (m/s^2)	C_v (J/kg·K)
Liquid	998	1.004×10^{-3}	9.81	0.007 28	4190
Gas	0	1.84×10^{-5}			1007

APPENDIX B: GRID INDEPENDENCE STUDY

Taking the tube with a size of 40 mm length and 3 mm inner diameter as an example, the grid convergence study is performed by developing three different meshes: coarse, medium, and fine grids. The number of cells and the simulation time for the three mesh conditions are listed in Table II. The simulation time listed in the table means the time cost of calculating bubble pulsation in 10 ms. Moreover, in all meshes, the near wall resolution is high enough to satisfy

TABLE II. Number of cells and CFD simulation time of three meshes.

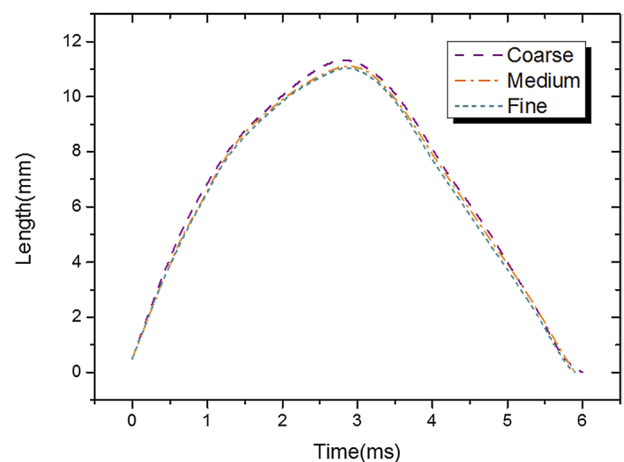| Mesh resolution	Coarse	Medium	Fine
Number of cells	603 372	1 003 392	1 211 860
Simulation time (36 CPU parallel)	4 h 10 min	6 h 9 min	8 h 24 min

FIG. 13. The temporal evolutions of the bubble's length in the first pulsation period with three different mesh conditions.

the need of the boundary layer since the y+ value is less than one. The temporal evolutions of the bubble's length during the first pulsation period using three meshes are shown in Fig. 13. The initial condition of the simulation is consistent with the typical case which is described in Sec. IV A.

As shown in Fig. 13, there are slight differences among three mesh conditions in the bubble's length in the first pulsation period, while the results of the medium mesh are quite close to the fine mesh. Since the simulation time is dependent on the number of cells, considering computational costs and efficiency, the medium mesh is further employed for the simulation of the tube with 40 mm length and 3 mm inner diameter. For other simulations of bubble pulsation in different sizes of tubes, the similar meshing resolution is applied and we ensure that the quality of mesh is reliable.

REFERENCES

[1]C.-D. Ohl, M. Arora, R. Dijkink, V. Janve, and D. Lohse, Appl. Phys. Lett. **89**(7), 074102 (2006).

[2]N. S. Yusof, B. Babgi, Y. Alghamdi, M. Aksu, J. Madhavan, and M. Ashokkumar, Ultrason. Sonochem. **29**, 568 (2015).

[3]D. L. Miller, G. J. Spooner, and A. R. Williams, J. Biomed. Opt. **6**(3), 351–358 (2001).

[4]P. R. Gogate and A. M. Kabadi, Biochem. Eng. J. **44**(1), 60–72 (2009).

[5]P. Senthil Kumar, M. Siva Kumar, and A. Pandit, Chem. Eng. Sci. **55**(9), 1633–1639 (2000).

[6]H. Jung Park and G. J. Diebold, J. Appl. Phys. **114**(6), 064913 (2013).

[7]X. Sheng, E. Kawakami, W. Hambleton, and R. Arndt, J. Fluids Eng. **133**(133), 57–64 (2010).

[8]E. Amromin, G. Karafiath, and B. Metcalf, J. Ship Res. **55**(3), 196–207 (2011).

[9]J. Wang, A. Abe, Y. Wang, and C. Huang, Ultrason. Sonochem. **42**, 541–550 (2018).

[10]Y. Huang, J. Wang, A. Abe, Y. Wang, T. Du, and C. Huang, Ultrason. Sonochem. **55**, 359–368 (2019).

[11]E. Zwaan, S. Le Gac, K. Tsuji, and C. D. Ohl, Phys. Rev. Lett. **98**(25), 254501 (2007).

[12]A. Heap and A. Juel, J. Fluid Mech. **633**, 485 (2009).

[13]T. W. Asegehegn, M. Schreiber, and H. J. Krautz, Chem. Eng. Sci. **66**(21), 5410–5427 (2011).

[14]M. Kornfeld and L. Suvorov, J. Appl. Phys. **15**(6), 495–506 (1944).

[15]A. Philipp and W. Lauterborn, J. Fluid Mech. **361**, 75–116 (1998).

[16]Y. X. Yang, Q. X. Wang, and T. S. Keat, Ultrason. Sonochem. **20**(4), 1098–1103 (2013).

[17]A. M. Zhang, S. Li, and J. Cui, Phys. Fluids **27**(6), 062102 (2015).

[18]E. A. Brujan, K. Nahen, P. Schmidt, and A. Vogel, J. Fluid Mech. **433**, 283–314 (2001).

[19]X. Ma, B. Huang, X. Zhao, Y. Wang, Q. Chang, S. Qiu, X. Fu, and G. Wang, Ultrason. Sonochem. **43**, 80–90 (2018).

[20]C. K. Turangan, G. P. Ong, E. Klaseboer, and B. C. Khoo, J. Appl. Phys. **100**(5), 054910 (2006).

[21]P. Koukouvinis, M. Gavaises, O. Supponen, and M. Farhat, Phys. Fluids **28**(5), 052103 (2016).

[22]P. Gregorčič, R. Petkovšek, and J. Možina, J. Appl. Phys. **102**(9), 094904 (2007).

[23]N. N. Liu, W. B. Wu, A. M. Zhang, and Y. L. Liu, Phys. Fluids **29**(10), 107102 (2017).

[24]A. M. Zhang, P. Cui, J. Cui, and Q. X. Wang, J. Fluid Mech. **776**, 137–160 (2015).

[25]X. J. Ma, T. Y. Xing, B. Huang, Q. H. Li, and Y. F. Yang, Ultrason. Sonochem. **40**, 480–487 (2018).

[26]O. Supponen, D. Obreschkow, M. Tinguely, P. Kobel, N. Dorsaz, and M. Farhat, J. Fluid Mech. **802**, 263–293 (2016).

[27]B. Han, Z. H. Shen, J. A. Lu, and X. W. Ni, Opt. Lasers Eng. **48**(10), 950–957 (2010).

[28]X. Wu, Y. Wang, and C. Huang, Chin. J. Theor. Appl. Mech. **47**(4), 687–698 (2015).

[29]Z. Z. Yin and A. Prosperetti, J. Micromech. Microeng. **15**(3), 643–651 (2005).

[30]S. S. Wang, Z. J. Jiao, X. Y. Huang, C. Yang, and N. T. Nguyen, Microfluid. Nanofluid. **6**(6), 847–852 (2009).

[31]S. Mitragotri, Nat. Rev. Drug Discovery **5**(7), 543–548 (2006).

[32]Y. Tagawa, N. Oudalov, C. W. Visser, I. R. Peters, D. van der Meer, C. Sun, A. Prosperetti, and D. Lohse, Phys. Rev. X **2**(3), 3573–3576 (2012).

[33]E. Ory, H. Yuan, A. Prosperetti, S. Popinet, and S. Zaleski, Phys. Fluids **12**(6), 1268–1277 (2000).

[34]C. Sun, E. Can, R. Dijkink, D. Lohse, and A. Prosperetti, J. Fluid Mech. **632**, 5 (2009).

[35]M. Xu, G. L. Hu, J. Zou, and C. Ji, Chin. J. Hydrodyn. **29**(4), 385–392 (2014).

[36]J. Zou, B. Li, and C. Ji, Exp. Therm. Fluid Sci. **61**, 105–112 (2015).

[37]C. Ji, B. Li, and J. Zou, Phys. Fluids **29**(8), 082107 (2017).

[38]B. Y. Ni, A. M. Zhang, Q. X. Wang, and B. Wang, Acta Mech. Sin. **28**(5), 1248–1260 (2012).

[39]G. Zhang, Y. Zhu, J. Yang, and M. Sun, Phys. Fluids **29**(6), 062102 (2017).

[40]S.-P. Wang, Q. Wang, A. M. Zhang, and E. Stride, Int. J. Multiphase Flow **121**, 103096 (2019).

[41]A. M. Zhang, B. Y. Ni, B. Y. Song, and X. L. Yao, Appl. Math. Mech. **31**(4), 449–460 (2010).

[42]M. Koch, C. Lechner, F. Reuter, K. Köhler, R. Mettin, and W. Lauterborn, Comput. Fluids **126**, 71–90 (2016).

[43]T. Li, S. Wang, S. Li, and A. M. Zhang, Appl. Ocean Res. **74**, 49–58 (2018).

[44]J. T. Huang and H. S. Zhang, Acta Mech. Sin. **23**(6), 645–653 (2007).

[45]S. Muller, M. Bachmann, D. Kroninger, T. Kurz, and P. Helluy, Comput. Fluids **38**(9), 1850–1862 (2009).

[46]V. Suponitsky, A. Froese, and S. Barsky, Comput. Fluids **89**(2), 1–19 (2014).

[47]Q. Zeng, S. R. Gonzalez-Avila, S. T. Voorde, and C.-D. Ohl, J. Fluid Mech. **846**, 916–943 (2018).

[48]H. Jasak, A. Jemcov, and Z. Tukovic, paper presented at the International Workshop on Coupled Methods in Numerical Dynamics/Terze, Zdravko; Lacor, Chris, 2007.

[49]X. Q. Wu, Q. M. Tan, and C. G. Huang, J. Appl. Phys. **114**(4), 043105 (2013).

[50]I. R. Peters, Y. Tagawa, N. Oudalov, C. Sun, A. Prosperetti, D. Lohse, and D. van der Meer, J. Fluid Mech. **719**, 587–605 (2013).

[51]B. Han, K. Köhler, K. Jungnickel, R. Mettin, W. Lauterborn, and A. Vogel, J. Fluid Mech. **771**, 706–742 (2015).

[52]Z. Yin, A. Prosperetti, and J. Kim, Int. J. Heat Mass Transfer **47**(5), 1053–1067 (2004).

[53]K. S. Suslick and D. J. Flannigan, Annu. Rev. Phys. Chem. **59**(1), 659 (2008).

[54]M. Dular and O. Coutier-Delgosha, J. Fluid Mech. **736**(736), 44–66 (2013).

[55]Y. F. Huang, L. C. Zhang, J. Chen, X. L. Zhu, Z. Liu, and K. P. Yan, Appl. Phys. Lett. **107**(18), 184104 (2015).

[56]A. H. Aghdam, B. C. Khoo, V. Farhangmehr, and M. T. Shervani-Tabar, Exp. Therm. Fluid Sci. **60**, 299–307 (2015).

[57]A. Vogel, J. Noack, K. Nahen, D. Theisen, S. Busch, U. Parlitz, D. X. Hammer, G. D. Noojin, B. A. Rockwell, and R. Birngruber, Appl. Phys. B **68**(2), 271–280 (1999).

[58]R. I. Issa, B. Ahmadi-Befrui, K. R. Beshay, and A. D. Gosman, J. Comput. Phys. **62**(1), 40–65 (1986).